

1 Studies of uniformity of 50 μm low-gain avalanche detectors
2 at the Fermilab test beam.

3 A. Apresyan^{*,a}, S. Xie^b, C. Pena^b, R. Arcidiacono^{e,g}, N. Cartiglia^e, M. Carulla^h,
4 G. Derylo^a, M. Ferrero^e, D. Flores^h, P. Freeman^d, Z. Galloway^d, A. Ghassemiⁱ, H. Al
5 Ghoul^c, L. Gray^a, S. Hidalgo^h, S. Kamadaⁱ, S. Los^a, M. Mandurrino^e, A. Merlos^h,
6 N. Minafra^c, G. Pellegrini^h, D. Quirion^h, C. Royon^c, H. Sadrozinski^d, A. Seiden^d,
7 V. Sola^e, M. Spiropulu^b, A. Staiano^e, L. Uplegger^a, K. Yamamotoⁱ, K. Yamamuraⁱ

8 ^aFermi National Accelerator Laboratory, Batavia, IL, USA

9 ^bCalifornia Institute of Technology, Pasadena, CA, USA

10 ^cUniversity of Kansas, KS, USA

11 ^dSCIPP, University of California Santa Cruz, CA, USA

12 ^eINFN, Torino, Italy

13 ^fUniversità di Torino, Torino, Italy

14 ^gUniversità del Piemonte Orientale, Italy

15 ^hCentro Nacional de Microelectrónica (IMB-CNM-CSIC), Barcelona, Spain

16 ⁱHamamatsu Photonics (HPK), Hamamatsu, Japan

17 **Abstract**

18 In this paper we report measurements of the uniformity of time resolution, signal am-
19 plitude, and charged particle detection efficiency across the sensor surface of low-gain
20 avalanche detectors (LGAD). Comparisons of the performance of sensors with different
21 doping concentrations and different active thicknesses are presented, as well as their tem-
22 perature dependance and radiation tolerance up to $6 \times 10^{14} \text{ n/cm}^2$. Results were obtained
23 at the Fermilab test beam facility using 120 GeV proton beams, and a high precision
24 pixel tracking detector. LGAD sensors manufactured by the Centro Nacional de Micro-
25 electrónica (CNM) and Hamamatsu Photonics (HPK) were studied. The uniformity of
26 the sensor response in pulse height before irradiation was found to have a 2% spread.
27 The efficiency and timing resolution before irradiation were found to be 100% and 30-
28 40 ps, respectively. A “no-response” area between pads was measured to be about 70 μm
29 for CNM and 110 μm for HPK sensors. After a neutron fluence of $6 \times 10^{14} \text{ n/cm}^2$ the
30 CNM sensor exhibits a large gain variation of a factor of 2.5 when comparing metallized
31 and non-metallized sensor areas. An irradiated CNM sensor achieved a time resolution
32 of 30 ps for the metallized area and 40 ps for the non-metallized area, while the HPK
33 sensor achieved a 30 ps time resolution.

34 **Key words:**

35 Silicon, Timing, LGAD

*Corresponding author

Email address: apresyan@fnal.gov (A. Apresyan)

³⁶	Contents		
³⁷	1	Introduction	2
³⁸	2	Experimental Setup	3
³⁹	3	LGAD Sensor Properties	5
⁴⁰	4	Readout Electronics	6
⁴¹	5	Sensor Studies and Analysis	7
⁴²	5.1	Study of the uniformity of the LGAD sensors	7
⁴³	5.2	Measurement of the “no-response” area between two neighboring pixels . .	9
⁴⁴	5.3	Comparison of HPK doping profiles	10
⁴⁵	5.4	Comparison of HPK 50 μm with 80 μm	13
⁴⁶	5.5	Temperature dependence of the LGAD sensors	15
⁴⁷	5.6	Radiation tolerance of the LGADs	18
⁴⁸	6	Conclusion	23

⁴⁹ 1. Introduction

⁵⁰ Future colliders, including the high luminosity upgrade of the Large Hadron Collider
⁵¹ (HL-LHC) at CERN, will operate with an order of magnitude higher instantaneous lu-
⁵² minosity compared to what has been achieved at the large hadron collider (LHC) so
⁵³ far. With the increased instantaneous luminosity, the rate of simultaneous interactions
⁵⁴ per bunch crossing (pileup) is projected to reach an average of 140 to 200. The large
⁵⁵ amount of pileup increases the likelihood of confusion in the reconstruction of particles
⁵⁶ from the hard scattering interaction with those produced in different pileup interactions.
⁵⁷ In particular, the ability to discriminate between jets produced in the events of inter-
⁵⁸ ests, especially those associated with vector boson fusion processes, and jets produced
⁵⁹ by pileup interactions will be degraded. Additionally, the efficiency to identify high p_{T}
⁶⁰ isolated electrons and muons will be severely reduced due to the high density of pileup
⁶¹ particles in their vicinity. The missing transverse energy resolution will also deteriorate,
⁶² and several other physics objects performance metrics will also suffer the detrimental
⁶³ effects of pileup.

⁶⁴ One way to mitigate the pileup effects mentioned above, complementary to precision
⁶⁵ tracking methods, is to perform a time of arrival measurement associated with each par-
⁶⁶ ticle. Such a measurement with a precision of about 20-30 ps, will reduce the effective
⁶⁷ amount of pileup by a factor of 10, given that the spread in collision time of the pileup
⁶⁸ interactions at HL-LHC is foreseen to be approximately 200 ps. We have previously
⁶⁹ shown that a precision of better than 20 ps can be achieved for electromagnetic showers
⁷⁰ measured with silicon sampling calorimeters [1–3] using traditional planar silicon detec-
⁷¹ tors. In this paper, we report results of particle beam measurements with thin low-gain
⁷² avalanche detectors (LGAD) that have been shown to achieve time resolutions around
⁷³ 30 ps [4]. LGAD are envisioned to be used in the CMS and ATLAS experiment upgrades
⁷⁴ for HL-LHC in order to reduce the pileup contamination. The implemented regions of

pseudorapidity (η) are: $|\eta| > 1.5$ and $|\eta| > 3.0$ for CMS and ATLAS, respectively. In order to achieve the desired timing precision across a large area of the detectors, the sensors will need to provide high uniformity of signal response and timing resolution. In this paper, we perform detailed measurements of the performance of LGAD sensors produced by Centro Nacional de Microelectrónica (CNM) and Hamamatsu Photonics (HPK) exposed to the 120 GeV proton beam at Fermilab. Utilizing high-precision tracking detectors we extract position dependence of the charged-particle detection efficiency, signal pulse height, signal timestamp, and time resolution. We also compare the performance of 50 and 80 μm LGAD sensors, as well as the HPK and CNM sensors irradiated to an equivalent neutron flux of $6 \times 10^{14} \text{ n/cm}^2$.

The paper is organized as follows: the experimental setup is described in Sec. 2; the tested LGAD sensors and their operating conditions are listed in Sec. 3; readout electronics used in the measurements are described in Sec. 4; beam test results are presented in Sec. 5, followed by the conclusion in Sec. 6.

2. Experimental Setup

Test-beam measurements were performed at the Fermilab Test-beam Facility (FTBF) which provided a 120 GeV proton beam from the Fermilab Main Injector accelerator. The Devices Under Test (DUTs) were mounted on a remotely operated motorized stage, placed inside the pixel telescope detector [5]. The latter provides better than 10 μm position resolution for charged particles impinging on the DUT. Additionally, a Photek 240 micro-channel plate (MCP-PMT) detector [6–9] was placed furthest downstream, and provided a very precise reference timestamp. Its precision has been previously measured to be less than 7 ps [8]. A schematic diagram and photograph of the experimental area are shown in Fig. 2 and Fig. 3, respectively.

The DAQ system for the DUTs and the Photek MCP-PMT is based on a CAEN V1742 digitizer board [10], which provides digitized waveforms sampled at 5 GS/s, and with one ADC count corresponding to 0.25 mV. The CAEN digitizer was voltage- and time-calibrated using the procedure described in Ref. [11]. The electronic time resolution of the CAEN V1742 digitizer was measured to be less than 4 ps, and thus, its impact on the timing measurements presented in these studies can be neglected. The DAQ for the pixel telescope is based on the CAPTAN system developed at Fermilab [5]. The track-reconstruction is performed using the Monicelli software package developed specifically for the test-beam application.

The beam is resonantly extracted in a slow spill for each Main Injector cycle delivering a single 4.2 sec long spill per minute. The primary beam (bunched at 53 MHz) consists of high energy protons (120 GeV) at variable intensities between 1 and 300 kHz. The trigger to both the CAEN V1742 and to the pixel telescope was provided by a scintillator mounted on a photomultiplier tube, placed upstream of the DUTs in the beam-line. Due to the limited buffer depth of the CAEN V1742 board, special care had to be taken in the design of the DAQ system to ensure that both the DUT and telescope DAQs collect exactly the same amount of triggers. This was achieved by limiting the trigger rate by introducing an adjustable dead-time using a custom-designed trigger board. This trigger board is the combination of a custom FPGA board (the CAPTAN+x, equipped with multiple FPGA Mezzanine Card connectors and gigabit ethernet connectivity) mated to a front end board (the NIM+, with multiple inputs and outputs, each supporting

120 a variety of interface levels such as NIM, LVDS, and TTL). The combined board is
 121 shown in Fig. 1 and was used to interface to photomultiplier signals through on-board
 122 programmable discriminators, and to form trigger signals with software configurable
 123 time-based veto and pre-scaler event filtering. We found that at a rate of about 1,500
 124 triggers per spill the CAEN V1742 and pixel telescope maintained full synchronization.
 125 Processed data from the pixel telescope and the DUTs were merged offline by matching
 126 the trigger counters recorded by the two systems.



Figure 1: The custom-made trigger board composed of NIM+ and CAPTAN+x boards.

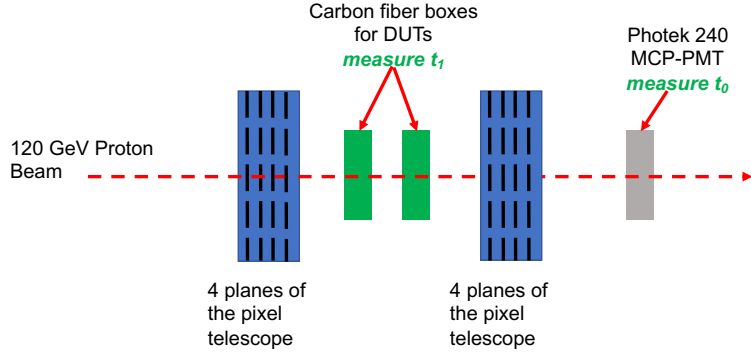


Figure 2: A schematic diagram of the test-beam setup is shown. The t_0 and t_1 are defined in Section 4.

127 The DUTs were placed inside the telescope box described in Ref.[5], and mounted on
 128 an aluminum mechanical support structure. The telescope box can be moved remotely
 129 in both the horizontal and vertical directions in order to align the DUTs with the beam.
 130 The aluminum support structure for the DUTs provide both mechanical stability and
 131 are equipped with Peltier cooling elements that were used in this study to operate the

₁₃₂ DUTs at -10° and -20° C.

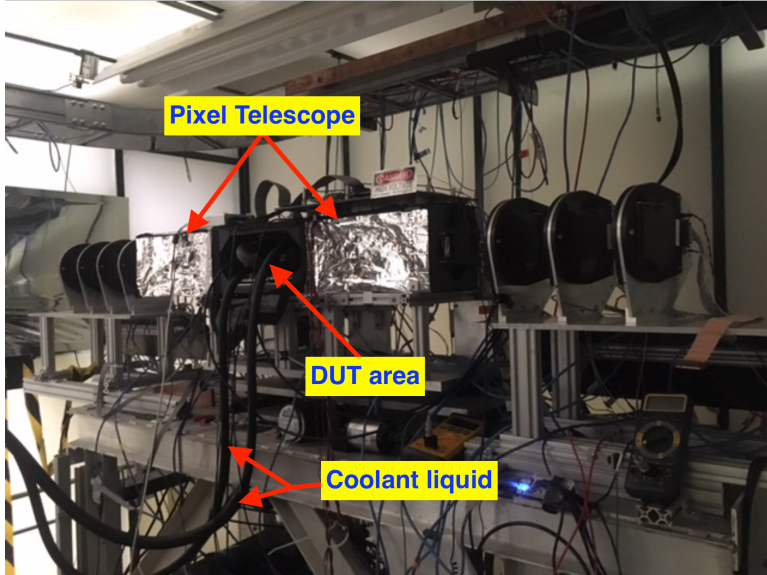


Figure 3: A picture of the experimental area. The pixel telescope detectors are placed inside the electrostatic-discharge shielded boxes on the two sides of the DUT area. Cooling liquid for the Peltier elements inside the DUT area is provided by the two tubes shown in the picture.

₁₃₃ 3. LGAD Sensor Properties

₁₃₄ Sensors manufactured by HPK and CNM were measured in the test beam experiment.
₁₃₅ Both single- and four-channel configurations of the sensor were used in the measurements.
₁₃₆ The sensors studied have active thicknesses of about $50\ \mu\text{m}$ and $80\ \mu\text{m}$.

₁₃₇ CNM sensors have an active thickness of about $45\ \mu\text{m}$ and were produced on 4-inch
₁₃₈ Silicon-on-Insulator wafers with a $45\ \mu\text{m}$ thick high resistivity float zone (FZ) active layer
₁₃₉ on top of a $1\ \mu\text{m}$ buried oxide and a $300\ \mu\text{m}$ support wafer. The back-side contact is
₁₄₀ achieved through wet-etched deep access holes through the insulator. Details on CNM
₁₄₁ sensors can be found in Ref. [4, 12].

₁₄₂ The HPK sensors were manufactured on 6-inch silicon wafers of $150\ \mu\text{m}$ total thickness
₁₄₃ with a $50\ \mu\text{m}$ or $80\ \mu\text{m}$ thick high resistivity float zone (FZ) active layer. Four gain splits,
₁₄₄ identified with the letters A (lowest gain) to D (highest gain), were produced identical
₁₄₅ in the mask design but with a different p^+ dose of the gain layer to study the optimal
₁₄₆ parameters of the charge multiplication mechanism. The pads were produced in three
₁₄₇ versions: two with guard ring (GR and GBGR) and one without guard ring. Four-channel
₁₄₈ sensors in a 2×2 array were produced with all 4 gain-splits, and are identified with the
₁₄₉ PIX identifier. For example, the 2×2 array of the $50\ \mu\text{m}$ sensor split D is labelled
₁₅₀ as 50D-PIX. The sensor corresponding to each of the four channels in the array is also
₁₅₁ referred to as a pixel in this paper. Each pixel in the 2×2 HPK array has dimensions
₁₅₂ of $3 \times 3\ \text{mm}^2$. The CNM single-channel sensors are square pads with an active area of

153 1.7 mm² while the HPK single-channel sensors are circular pads with an active area of
154 0.8 mm².

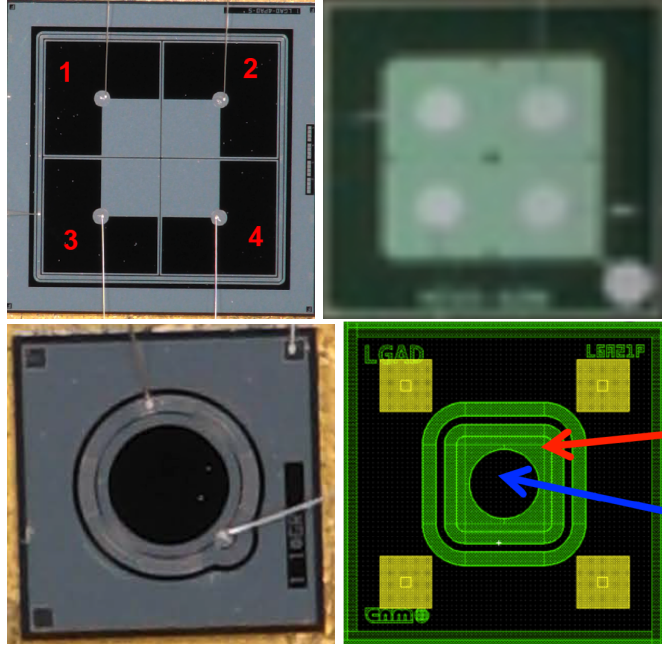


Figure 4: Photographs of the HPK 50D-PIX 2 × 2 array sensor (top left), the CNM-W9HG11 2 × 2 array sensor (top right), the 50D-GR single sensor (bottom left), and the CNM W11LGA35 single sensor (bottom right) are shown. The pixel labels overlaid on top of the array sensors are used in the text to identify pixels on the array. Signals from the pixels are read out by the micro-bonds that are connected to the signal pads on the sensors. **FIXME better quality images for CNM sensors**

155 4. Readout Electronics

156 Three readout electronics boards were used in various measurements presented in this
157 paper. They were independently developed at Fermi National Accelerator Laboratory
158 (FNAL), at the University of Kansas (KU), and at the University of California Santa
159 Cruz (UCSC).

160 The 4-channel Fermilab LGAD test board is designed to test sensors up to 8.5 mm
161 by 8.5 mm at voltages up to 1 kV. Four wire-bonding pads allow for signal readout
162 via amplifiers based on Mini-Circuits GALI-66+. The amplifiers feature transformers
163 with 1:2 input impedance matching, two stages of amplification and a 500 MHz low-
164 pass filter. In this full configuration, the amplifiers feature 12.5 Ω input impedance, 5 kΩ
165 transimpedance, 500 MHz bandwidth and 1 mV rms output noise. If needed it is possible
166 to jump the input transformer and/or the low-pass filter, which would result in an input
167 impedance of 50 Ω, transimpedance of 10 kΩ, and bandwidth of 2 GHz.

168 The 2-channel KU board, designed and produced by the University of Kansas, can
169 accommodate many types of sensors including diamond, silicon, LGAD or avalanche
170 photodiodes (APD). The sensor is hosted on the board itself and the electronics was

171 optimized for precise timing measurements. In particular, the amplifier, made with
172 discrete components, has an input impedance of $700\ \Omega$, an output noise of 4 mV and a
173 gain in transresistance of about $50\text{ mV}/\mu\text{A}$ with a 3 dB bandwidth of 100 MHz. Those
174 values were simulated for an input capacitance of 20 pF, which corresponds roughly to
175 an LGAD of 9 mm^2 . The power consumption of the board is about 130 W per channel.

176 The UCSC 1-channel board is described in detail in Ref. [4]. This board uses discrete
177 components and contains several features which allow for maintaining a wide bandwidth
178 ($\sim 2\text{ GHz}$) and a low noise even in noisy environments. The inverting amplifier uses a
179 high-speed SiGe transistor which has a transimpedance of about $470\ \Omega$. A commercial
180 inverting amplifier with gain 10x is used to boost the signal. The 4-channel UCSC board
181 has two stages: the first one is identical to the UCSC single channel board, and is followed
182 by an inverting stage. The total transimpedance is $10.7\text{ k}\Omega$.

183 5. Sensor Studies and Analysis

184 We present a number of different studies performed on the LGAD sensors described
185 in Section 3. They include signal response uniformity, gap distance between adjacent
186 pixels, doping profile and sensor thickness characterization, temperature and irradiation
187 dependence, and timing resolution. A brief overview of the analysis methods is given
188 below, followed by subsections describing the details and results of each study.

189 As discussed in Section 2, the reference time is measured using the Photek MCP-
190 PMT detector. The timestamp for this reference detector is obtained by fitting the peak
191 region of the pulse to a Gaussian function and the mean parameter of the Gaussian is
192 assigned as the timestamp t_0 . The timestamp for signals from the LGAD sensors is
193 obtained in two different ways depending on which read-out board was used. For the
194 KU board, which has a slower decay time, the timestamp is obtained by performing
195 a linear fit to the rising edge of the pulse and the time at which the pulse reaches 45%
196 of the maximum amplitude is assigned as its timestamp t_1 . For the FNAL and UCSC
197 boards, which have fast decay times, the timestamp is obtained via a fit to a Gaussian
198 function analogous to what is done for the reference detector.

199 Events are required to have a signal in the Photek MCP-PMT consistent with a
200 minimum ionizing particle (MIP), and a signal above the noise in LGAD sensors. The
201 MIP signal selection in the Photek MCP-PMT is the same for all runs and requires that
202 the signal amplitude is between 160 mV and 320 mV. The signal selection for LGAD
203 boards was optimized for each board individually, by selecting the MIP signal peak fitted
204 with a Landau function. All measurements other than those described in Sec. 5.5 and
205 5.6 were performed at room temperature.

206 Here, and in the remainder of this article, whenever a scan of a certain characteristic
207 quantity – e.g. time resolution – of the sensor is presented, we show the X-axis scan for
208 pixels 1 and 2, and the Y-axis scan for pixels 1 and 3, as defined on the left picture in
209 Fig. 4. The X-axis scan across pixels 3 and 4, and Y-axis scan across pixels 2 and 4 show
210 qualitatively the same features, and are not presented here.

211 5.1. Study of the uniformity of the LGAD sensors

212 We present in detail uniformity studies – including signal detection efficiency, most
213 probable value, time difference, and time resolution – accross the sensitive area of the

LGAD. The sensors under study were produced by HPK and CNM. The largest dataset was collected for the HPK 50D-PIX sensor and the CNM W9HG11 sensor as they were the best performing sensors from HPK and CNM respectively. The HPK 50D-PIX sensor was mounted on the 4-channel FNAL board and biased to -300 V, while the CNM W9HG11 sensor was mounted on the 4-channel UCSC board and biased to -180 V. Both sensors were operated at the room temperature for these studies.

The measurements of the particle detection efficiency are shown in Fig. 5. Efficiency is defined as the ratio of events that register a signal above the noise level in the LGAD sensor to those that contain a track identified by the pixel telescope pointing at the LGAD sensor. We observe a flat 100% efficiency across the whole sensor area. The left edge in the X-axis scan of pixel 1 on HPK 50D-PIX sensor in Fig. 5 is outside the acceptance of the pixel telescope, hence the efficiency curve does not fully cover its surface. A clear drop in efficiency is observed in the transition (“no-response”) region between the two pixels. A more detailed study of the “no-response” region is given in Sec. 5.2.

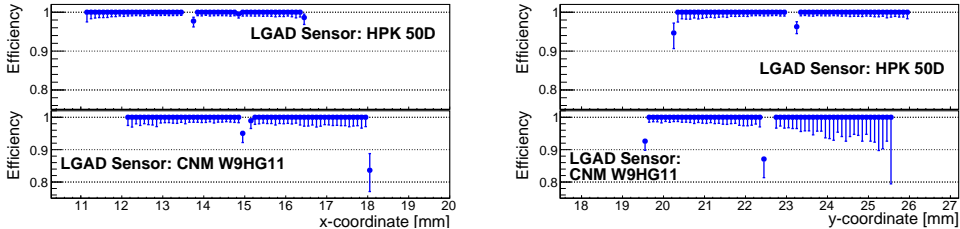


Figure 5: Efficiency measurement across the X-axis (left) and Y-axes (right) of the HPK 50D-PIX sensor mounted on the FNAL board, and the CNM W9HG11 sensor mounted on the UCSC board. The scans of pixels 1 and 2 along the X-axis, and pixels 1 and 3 along the Y-axis are shown. The pixel numbering scheme is defined in Fig. 4.

An important characteristic is the uniformity of the signal size across the surface of the sensor, which directly impacts its timing performance. We use the signal amplitude as the metric to characterize the signal size uniformity. The distribution of the LGAD signal amplitudes is fit to a Landau distribution. The most probable value (MPV) parameter of the fitted Landau distribution is plotted in Fig. 6. A flat response with a uniform signal size is observed over the whole sensor area.

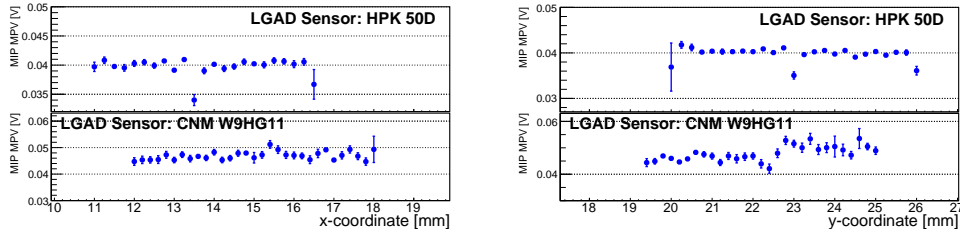


Figure 6: Signal amplitude MPV measurement across the X-axis (left) and Y-axes (right) of the HPK 50D-PIX sensor mounted on the FNAL board, and the CNM W9HG11 sensor mounted on the UCSC board. The scans of pixels 1 and 2 along the X-axis and pixels 1 and 3 along the Y-axis are shown. The pixel numbering scheme is defined in Fig. 4.

234 The measurements of the time difference $\Delta t = t_1 - t_0$ between the reference timestamp
 235 (t_0) and the timestamp of the LGAD sensors (t_1) are shown in Fig. 7. The micro-bonding
 236 scheme of the HPK PIX 2×2 sensor arrays is shown in Fig. 4, and **FIXME NEED**
 237 **to add CNM array image similar to HPK one.** For the HPK sensor, the Δt
 238 dependence on the hit position indicates a shift of about 20–30 ps between the metallized
 239 area near the center of the array (gray region of the top-left image in Fig. 4) and the
 240 non-metallized area. A possible explanation for this effect is a small difference in the rise
 241 time of the pulses between the metallized and non-metallized areas. The results for the
 242 CNM sensor also show hints of this behavior, though the larger statistical uncertainties
 243 make it less significant.

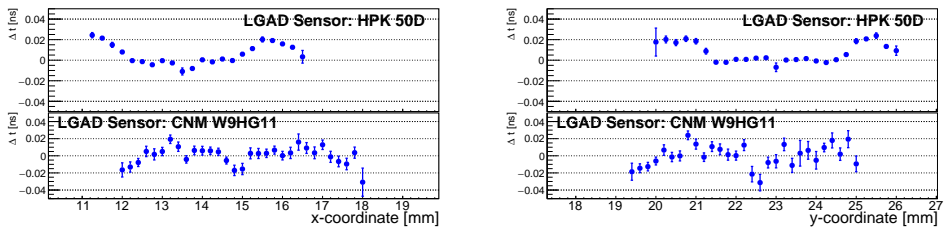


Figure 7: Δt measurement across the X- and Y-axes of the HPK 50D-PIX sensor mounted on the FNAL board. The scans of pixels 1 and 2 along the X-axis, and pixels 1 and 3 along the Y-axis are shown. The pixel numbering scheme is defined in Fig. 4.

244 The measurement of the time resolution across the sensor surface is shown in Fig. 8.
 245 The distribution of Δt between the timestamp of the LGAD signal and the reference
 246 signal is fitted with a Gaussian function, and the spread σ of the fitted function is
 247 defined as the time resolution. We observe a uniform time resolution around 40 ps across
 248 the whole surface area for HPK, and around 55 ps for CNM sensors.

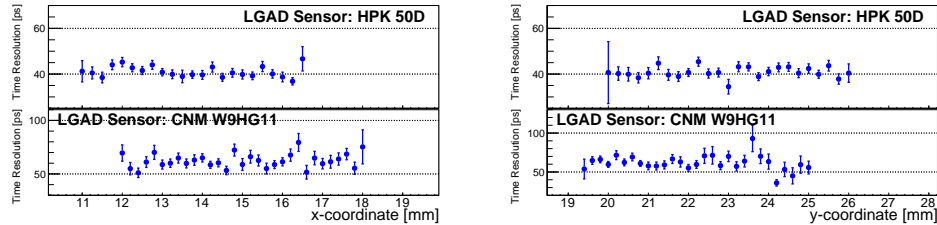


Figure 8: Time resolution measurement across the X-axis (left) and Y-axes (right) of the HPK 50D-PIX sensor mounted on the FNAL board, and the CNM W9HG11 sensor mounted on the UCSC board. The scans of pixels 1 and 2 along the X-axis, and pixels 1 and 3 along the Y-axis are shown. The pixel numbering scheme is defined in Fig. 4.

249 5.2. Measurement of the “no-response” area between two neighboring pixels

250 In order to precisely measure the width of the no-response area between two neigbor-
 251 boring pixels, a large statistics sample of about 350,000 events was collected with the
 252 HPK 50D-PIX sensor mounted on a 2-channel KU board. The sensor was biased to
 253 -300 V. The large dataset allowed us to perform a detailed scan in the area between

254 the two pixels as shown in Fig. 9. In order to estimate the width of the no-response
 255 between the pixels, the efficiency curves of the two neighboring pixels are fitted with an
 256 S-curve function of the form $y = p_1 \times \text{erf}\{\pm(p_2 - x)/p_3\} + p_4$, where erf is the error
 257 function, and p_i are floated in the fit. We define the width of the “no-response” area as
 258 the distance between the half-maxima of the two fitted S-curves, as shown in Fig. 9. We
 259 measure the width of the no-response area on the HPK 50D-PIX sensor to be $110 \mu\text{m}$,
 260 with an uncertainty of $10 \mu\text{m}$.

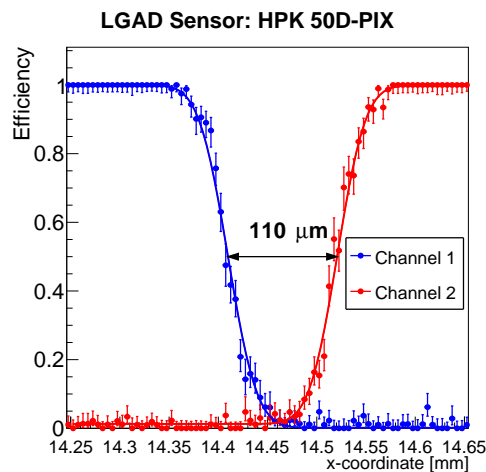


Figure 9: A zoom-in version of the efficiency measurement as a function of the X position of the beam particle. The HPK 50D-PIX sensor was operated at -300 V bias voltage. The pixel numbering scheme is defined in Fig. 4.

261 A further measurement was made on the 4-channel UCSC board for the HPK 50C-
 262 PIX sensor and the CNM W9HG11 sensor. We compare the width of the gap region of
 263 the HPK and CNM sensors in Fig. 10. Both sensors in this comparison were tested in
 264 the beam simultaneously. The HPK 50C-PIX sensor was operated at -450 V , and CNM
 265 W9HG11 sensor was operated at -180 V . We measure the size of the “no-response”
 266 region to be around $110 \mu\text{m}$ on the HPK 50C-PIX – compatible with the HPK 50D-PIX
 267 sensor – and around $70 \mu\text{m}$ for the CNM sensor. Both measurements have an uncertainty
 268 of $10 \mu\text{m}$.

269 5.3. Comparison of HPK doping profiles

270 Studies of the dependence of the sensors’ characteristics on the doping concentrations
 271 were performed by comparing the $50 \mu\text{m}$ HPK PIX sensors of different gain splits.
 272 In order to reduce the impact of the variations between different readout boards, all
 273 measurements presented in this section were performed using only 2-channel KU readout
 274 boards. Four readout boards were prepared, each with an HPK sensor mounted on it, and
 275 tested in the beam. Data taken with the HPK 50D-PIX is the same as that presented
 276 in Fig. 9, which is the largest data sample collected during this test beam campaign.
 277 Therefore, the statistical uncertainties in the measurements of the HPK 50A-, B-, and
 278 C-PIX sensors are larger than those of 50D-PIX. For this study, the sensors were oper-
 279 ated at room temperature, and their bias voltages were set to -630 V , -550 V , -400 V ,

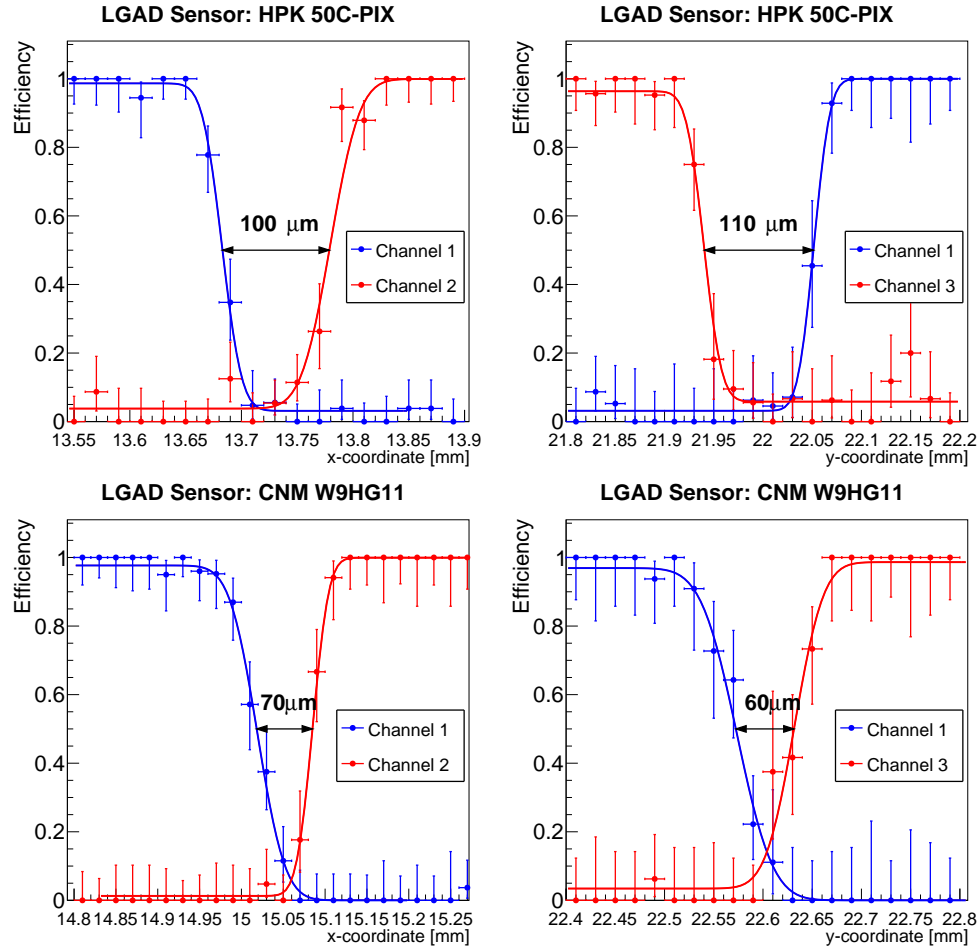


Figure 10: A zoom-in version of the efficiency measurement across the X- and Y-axes of the HPK 50C-PIX (top) and CNM W9HG11 (bottom) sensors. HPK sensor is operated at -450 V, and CNM sensor is operated at -180 V. Data points in blue are those from one pixel, and data points in red are from the neighboring pixel. The blue and red curves are fitted to the data points as described in the text. Arrows indicate the distance between the half-maximum points of the fitted curves.

280 and -300 V for the HPK 50A-PIX, HPK 50B-PIX, HPK 50C-PIX, and HPK 50D-PIX
281 sensors, respectively.

282 The distribution of the MPV of signal amplitudes across the sensor area is shown
283 in Fig. 11, where the MPV is extracted as described in Sec. 5.1. Comparing the signal
284 amplitudes between the two pixels one observes that the gain varies between the two
285 channels. However, comparing the MPV distribution of the HPK 50D-PIX sensors shown
286 in Fig. 11 with the one shown in Fig. 6, it is clear that the observed difference in gain
287 among these two channels is not due to variations in the sensor properties but rather
288 imperfections in the reaout board. The differences in the signal size between two channels
289 on the KU board are attributed to imperfections in the manufacturing process of the
290 custom-designed pre-amplifiers used in the boards. Nevertheless, signal MPV within a
291 single pixel is highly uniform for all tested samples.

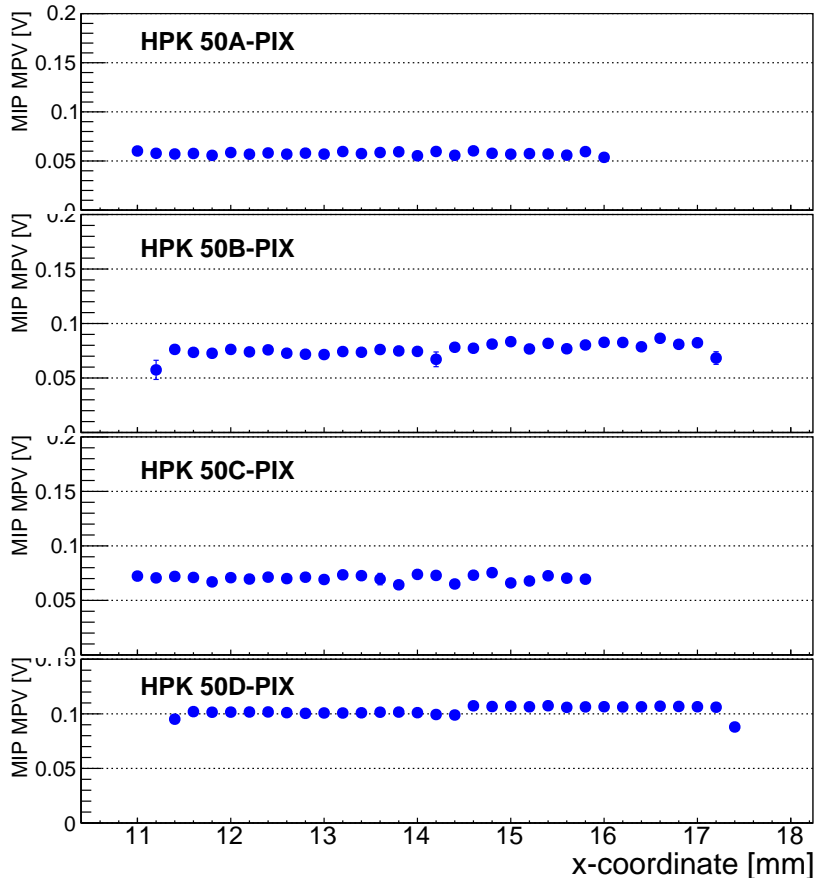


Figure 11: Signal amplitude MPV measurement across the X-axis of the HPK 50A-, 50B-, 50C-, and 50D-PIX sensors mounted on the KU board. The scan of pixels 1 and 2 along the X-axis, and pixel numbering scheme is defined in Fig. 4.

292 The measurements of the time difference between the reference timestamp and the
293 timestamps of the HPK sensors are shown in Fig. 12. As was shown in Fig. 7, the Δt

294 exhibits an offset of about 20 ps between the metalized area and the non-metalized area
 295 of the sensor. The feature is present in all 4 types of the HPK PIX sensors and appear
 296 to be statistically consistent in shape and magnitude.

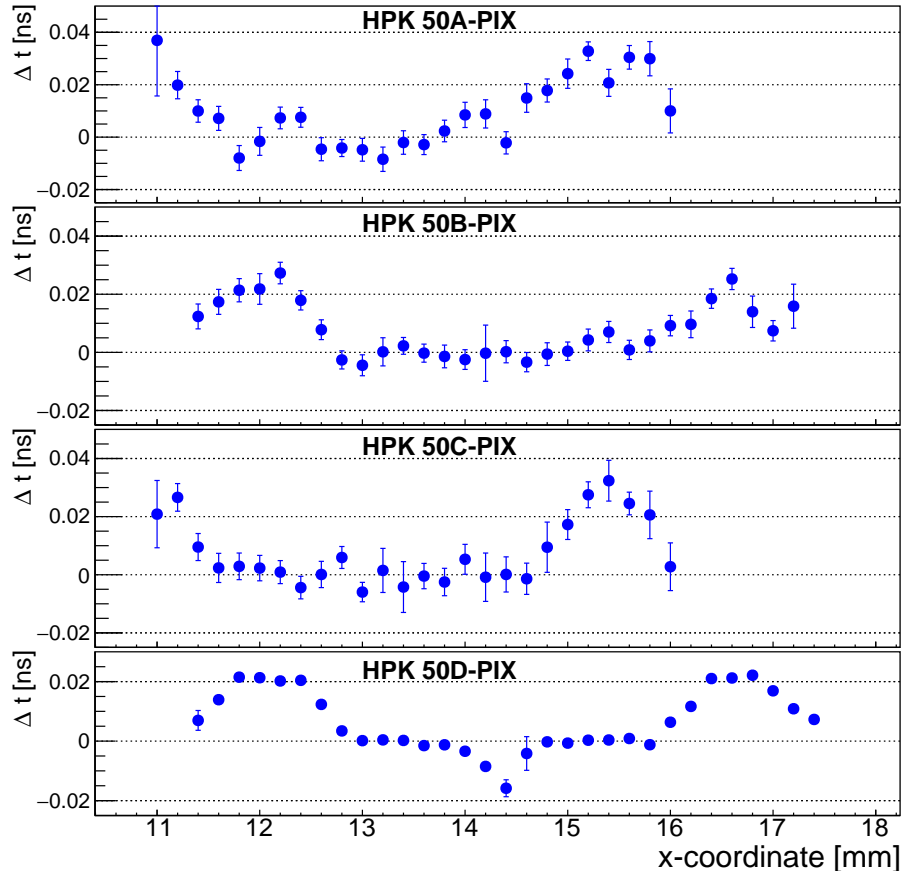


Figure 12: Δt measurements as a function of the X position of the beam particle for the HPK 50A-, 50B-, 50C-, and 50D-PIX sensors mounted on the KU board. The scan of pixels 1 and 2 along the X-axis is shown. The pixel numbering scheme is defined in Fig. 4.

297 The measurements of the time resolution across the sensors are shown in Fig. 13. We
 298 observe a uniform time resolution around 40 ps across the entire sensor area. **FIXME**
 299 explanation for the difference in resolution on two pixels of A and C. I suspect
 300 this is due to difference in gain in two pre-amps on KU board.

301 5.4. Comparison of HPK 50 μm with 80 μm

302 The thickness of the active area of the sensor is an important design parameter when
 303 optimizing for time resolution. A thicker sensor will result in a larger signal size and will
 304 generally improve the time resolution. However, a thicker sensor also increases the size
 305 of Landau fluctuations which will tend to degrade the time resolution. Therefore, it is

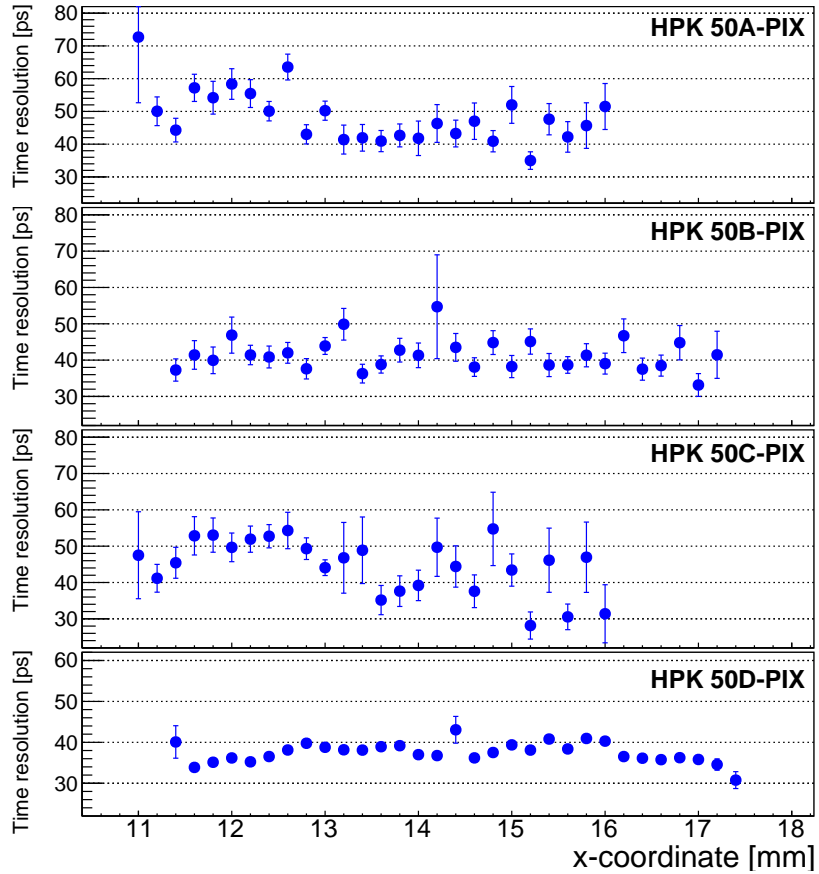


Figure 13: Time resolution measurements as a function of the X position of the beam particle for the HPK 50A-, 50B-, 50C-, and 50D-PIX sensors mounted on the KU board. The scan of pixels 1 and 2 along the X-axis is shown. The pixel numbering scheme is defined in Fig. 4.

306 an interesting study to understand whether increasing the sensor thickness – from 50 μm
307 to 80 μm – will have any impact on the measured time resolution.

308 This study is performed using the HPK C-PIX sensors with the same dopant concen-
309 tration. The 80 μm sensor HPK 80C-PIX is biased at -610 V, while the 50 μm sensor
310 HPK 50C-PIX is biased at -400 V. The time resolution for the two sensors are shown in
311 Fig. 14 as a function of position, and exhibit fairly uniform behavior. The measured time
312 resolutions range from 40 ps to 50 ps and are relatively similar for these two different
313 sensor thicknesses. **WHAT READOUT BOARD DID WE USE HERE?**

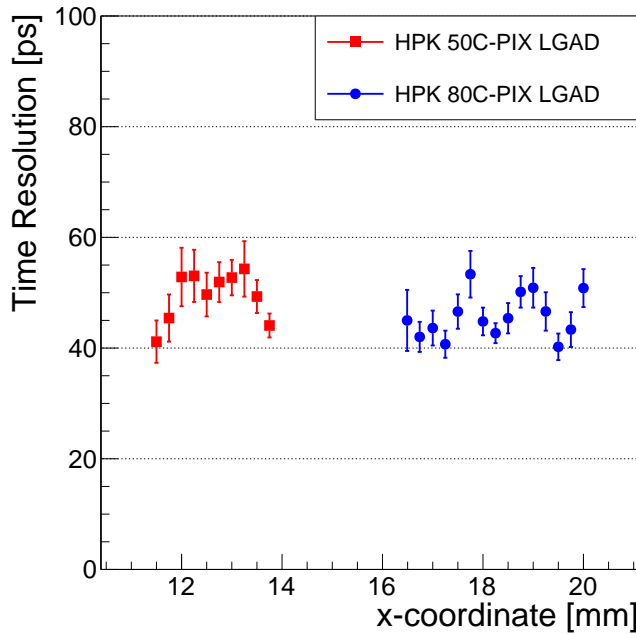


Figure 14: Comparison of time resolution in FNAL 80C versus KU 50C sensors

314 *5.5. Temperature dependence of the LGAD sensors*

315 In order to maintain their optimal performance at the highest fluences envisioned at
316 the HL-LHC, the LGAD sensors will be cooled to temperatures below -20°C degrees.
317 Operation at such low temperatures will allow to significantly reduce the leakage current,
318 and additionally improve the timing characteristics of the sensors. In this section we de-
319 scribe the measurements of the LGAD sensors performed at -10 and -20°C degrees, and
320 compare the results to those at room temperature. These measurements were performed
321 with the HPK 50D-PIX sensors mounted on the FNAL 4-channel board. The sensor was
322 biased at the same voltage of -250 V for all temperature scenarios.

323 The distribution of the signal MPV across the sensor surface is shown in Fig. 15. We
324 observe that the signal MPV increases by more than a factor of two when the temperature
325 is reduced from $+20^\circ\text{C}$ to -20°C . While the MPV uniformity across the two channels

326 are within 2% of each other at room temperature, at lower temperatures one of the pixels
 327 shows a difference of about 5% with respect to its neighboring pixel. A more detailed
 328 study is needed to understand whether this difference is due to non-uniform temperature
 329 distribution across the sensor array or due to differences in the signal response between
 330 different pixel sensors at colder temperatures.

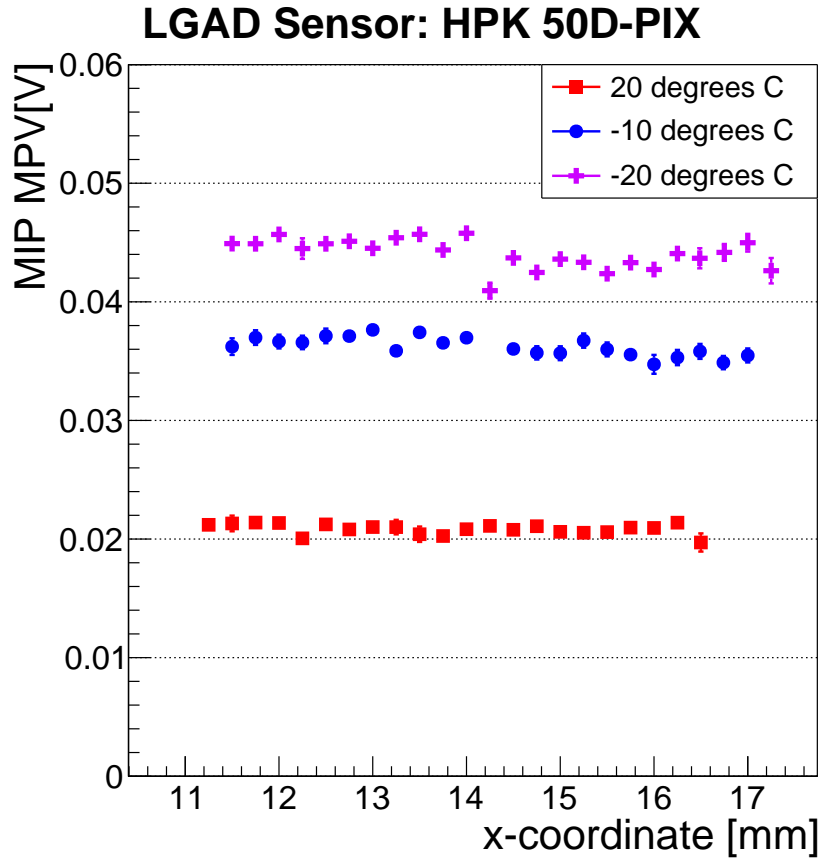


Figure 15: Temperature dependence of the signal amplitude MPV uniformity across the X-axis of the HPK 50D-PIX sensors mounted on the FNAL board. The scan of pixels 1 and 2 along the X-axis is shown, and pixel numbering scheme is defined in Fig. 4. The HPK sensor is biased at -250 V.

331 The distribution of the Δt between the reference timestamp and the timestamp from
 332 the HPK 50D-PIX sensor is shown in Fig. 16. We observe no significant changes in the
 333 behavior of the Δt as the temperature varies.

334 The time resolution measured for the HPK 50D-PIX sensor is shown in Fig. 17. We
 335 observe a significant improvement in the time resolution as the temperature is lowered
 336 from $+20^{\circ}\text{C}$ to -20°C degrees. As the temperature is lowered, the signal-to-noise ratio
 337 improves as the gain of the LGAD sensor increases and the electronics noise decreases.
 338 The noise was observed to remain relatively constant at 1.2 mV for both $+20$ and -20°C .
 339 Therefore the improvement comes mainly from the increase in the signal gain. The time

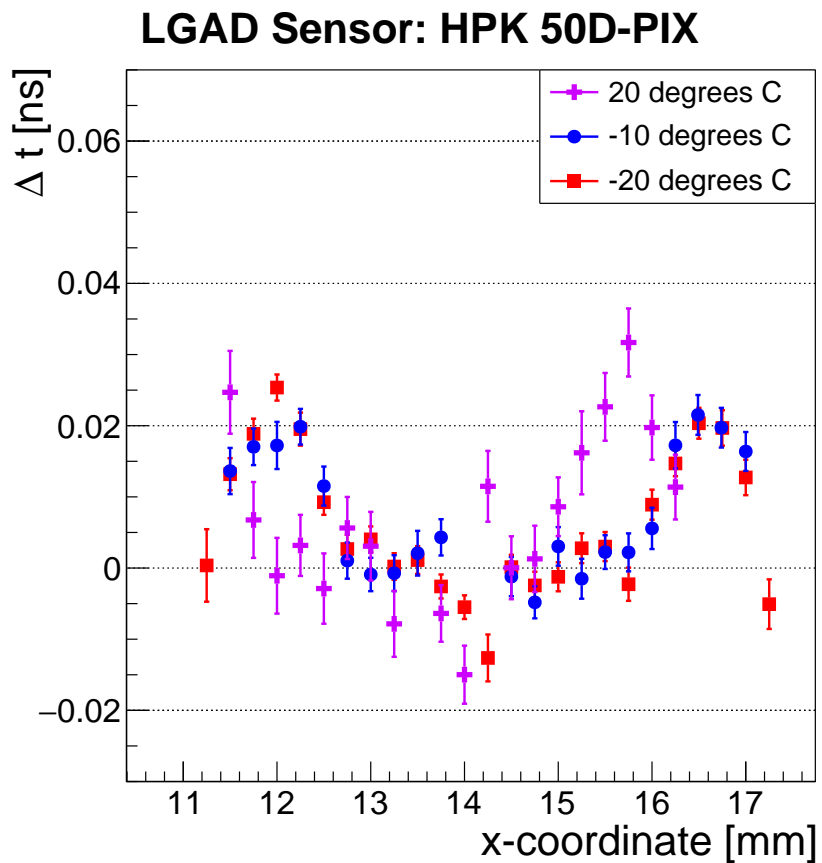


Figure 16: Temperature dependance of the Δt uniformity across the X-axis of the HPK 50D-PIX sensors mounted on the FNAL board. The scan of pixels 1 and 2 along the X-axis is shown, and pixel numberng scheme is defined in Fig. 4. The HPK sensor is biased at -250 V.

³⁴⁰ resolution was measured to improve from around 55-60 ps at the room temperature,
³⁴¹ down to 35-40 ps at -20°C .

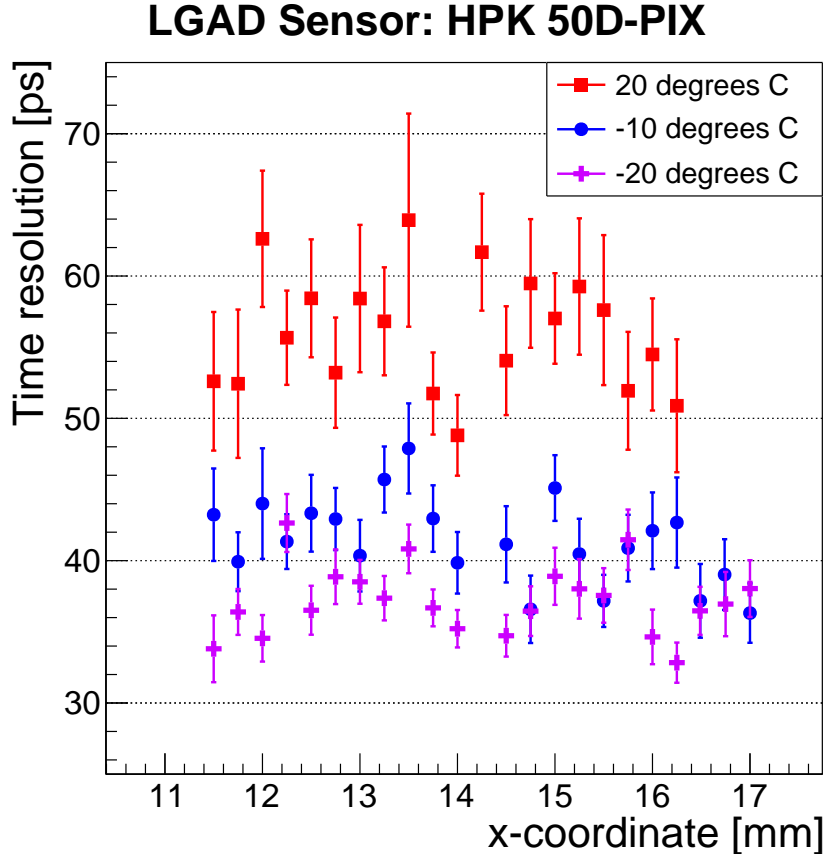


Figure 17: Temperature dependance of the time resolution uniformity across the X-axis of the HPK 50D-PIX sensors mounted on the FNAL board. The scan of pixels 1 and 2 along the X-axis is shown. The pixel numberng scheme is defined in Fig. 4. The HPK sensor is biased at -250 V .

³⁴² 5.6. Radiation tolerance of the LGADs

³⁴³ In this section we present the studies of the irradiated HPK and CNM sensors, which
³⁴⁴ were exposed to neutron irradiation at the Ljubljana TRIGA reactor. The neutron
³⁴⁵ spectrum and flux are well known and the fluence is quoted in 1 MeV equivalent neutrons
³⁴⁶ per cm^2 ($n_{\text{eq}}/\text{cm}^2$ or n/cm^2 for short). After $6 \times 10^{14} \text{ n}/\text{cm}^2$ irradiation, the devices
³⁴⁷ were annealed for 80 min at 60°C . Afterward the devices were kept at -20°C degree
³⁴⁸ during storage, transportation, and test beam experiments.

³⁴⁹ The two-dimensional distribution of the signal amplitudes on the surface of the ir-
³⁵⁰ radiated sensors are shown in Figs. 18 and 19. From the comparison with the image
³⁵¹ of the CNM sensor shown in Fig. 4 and the distribution in Fig. 18, it is clear that two

352 distinct regions can be identified on the sensor based on the signal amplitude: the region
 353 under the aluminum metallization on the periphery of the sensor, and the region without
 354 aluminum metallization in the center. The distribution on the right of Fig. 18 shows
 355 that the amplitude under the aluminum (periphery) is about 2.5 times larger than that
 356 without aluminum (center). The amplitude scan of the irradiated HPK 50D sensor is
 357 shown on the left panel of Fig. 19, and a uniform amplitude across the sensor surface is
 358 observed, which can also be seen on the right panel of Fig. 19. In contrast to the CNM
 359 sensor, the HPK sensor does not contain any portions that have active area covered with
 360 aluminum metallization.

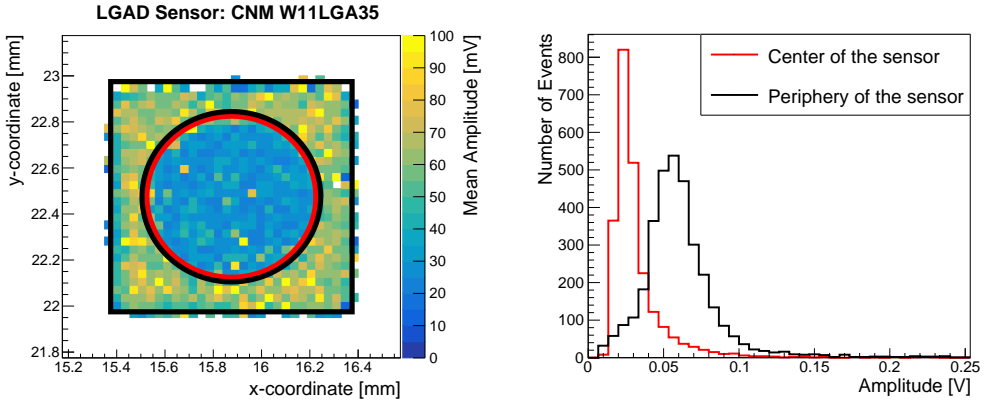


Figure 18: (Left) The map of the amplitude distribution on the irradiated CNM W11LGA35 sensor across X and Y coordinates. Two distinct regions on the sensor surface can be identified according to the amplitude distribution: the center of the sensor (area within the red circle), and the periphery of the sensor (area between the black circle and black square). (Right) Amplitude distribution in the two areas of the irradiated CNM W11LGA35 sensor. The sensor was irradiated to $6 \times 10^{14} \text{ n/cm}^2$. Measurements were performed at -20°C .

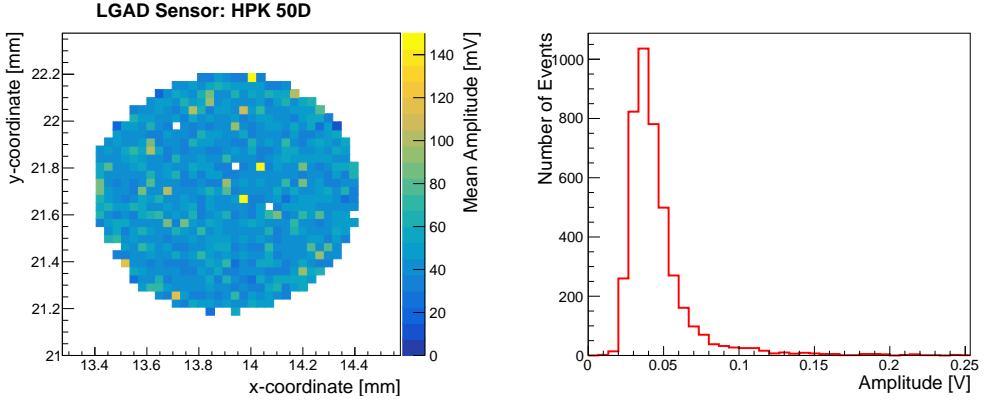


Figure 19: (Left) The map of the amplitude distribution on the irradiated HPK 50D sensor across X and Y coordinates. (Right) Signal amplitude distribution for the irradiated HPK 50D sensor. The sensor was irradiated to $6 \times 10^{14} \text{ n/cm}^2$. Measurements were performed at -20°C .

361 Measurements of the particle detection efficiency are shown in Fig. 20. These mea-
 362 surements were performed with the HPK sensor biased at -600 V, and the CNM sensor
 363 biased at -400 V. We observe a flat 100% efficiency across the whole HPK sensor area,
 364 and the efficiency of the CNM sensor is also very close to 100%. As with the pixelated
 365 array sensors, a clear drop in efficiency is observed near the edges of the active area.

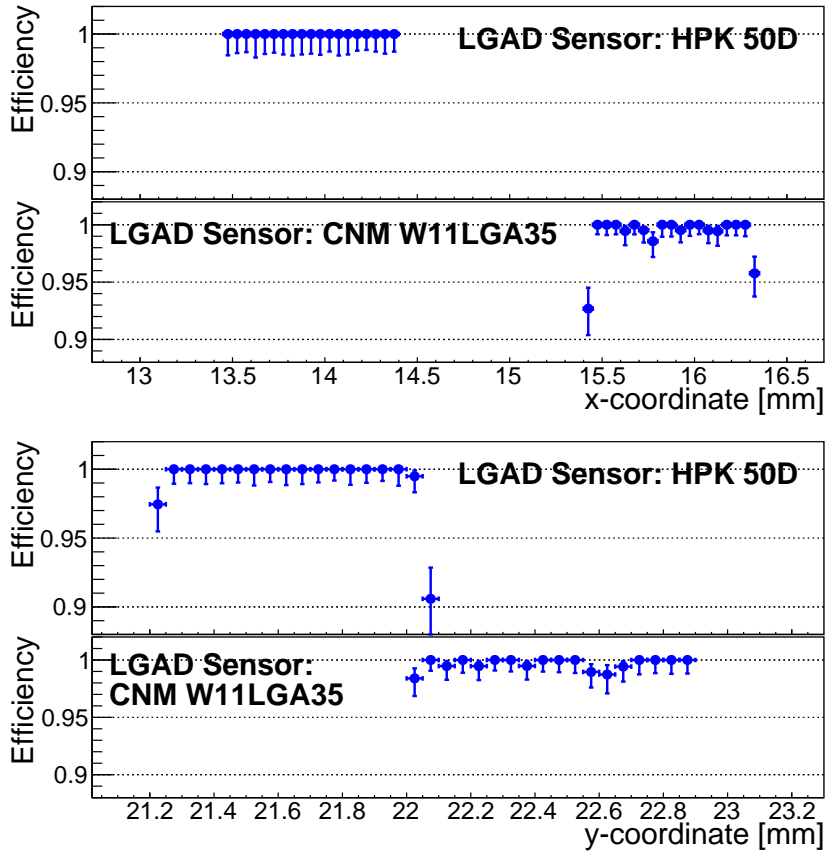


Figure 20: Efficiency measurements across the X-axis (top) and Y-axes (bottom) of the HPK 50D and CNM W11LGA35 irradiated sensors. Both sensors were irradiated to 6×10^{14} n/cm². Measurements were performed at -20°C .

366 The distribution of MPV of signal amplitudes across the sensor area is shown in
 367 Fig. 21, where the MPV is extracted as described in Sec. 5.1. surements were performed
 368 at two bias voltage values for both sensors: -600 and -635 V for HPK, and -400
 369 and -420 V for CNM sensors. **FIXME HARTMUT what are the gains at these**
 370 **voltage values?**. A uniform signal amplitude is observed across the HPK sensor, while
 371 for the CNM sensor the amplitude varies across the sensor surface, as observed also in
 372 Fig. 18.

373 The distribution of the Δt between the reference timestamp and the timestamps of the
 374 signals from the irradiated HPK and CNM sensors are shown in Fig. 22. Measurements

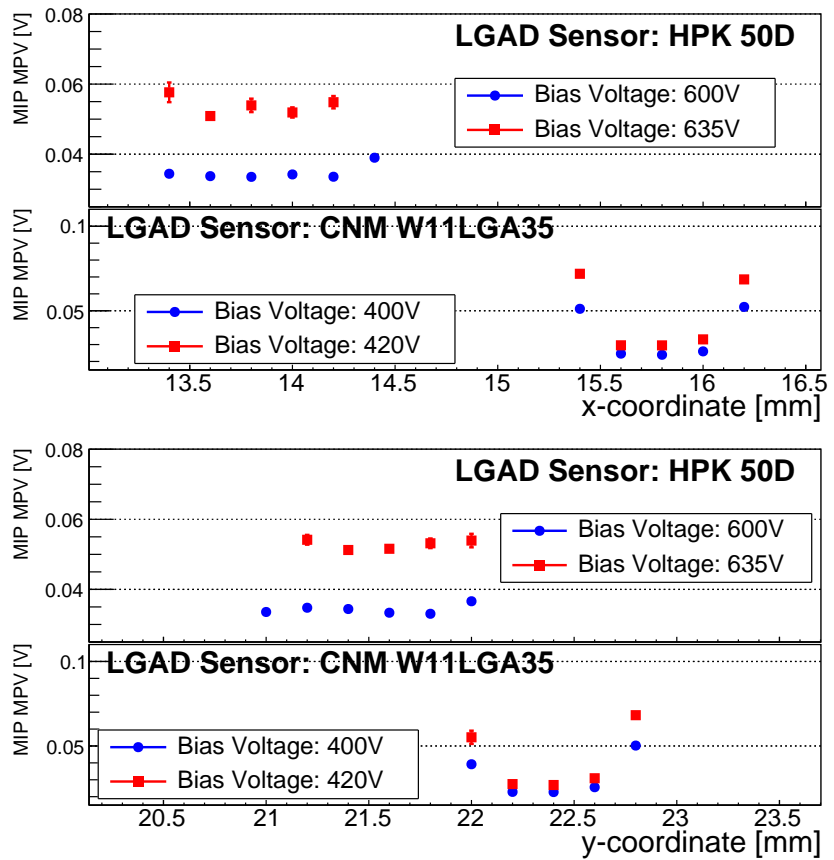


Figure 21: Signal amplitude MPV measurement across the X-axis (top) and Y-axes (bottom) of the HPK 50D and CNM W11LGA35 irradiated sensors. Both sensors were irradiated to $6 \times 10^{14} \text{ n/cm}^2$. Measurements were performed at -20°C .

375 at both bias voltage values are presented. We measured a uniform distribution of the
 376 Δt values across the HPK sensor. The CNM sensor exhibits a non-uniformity across
 377 the sensor surface, where the signals from the central, non-metallized area arrive are
 378 about 10 ps faster than those from the peripheral, metallized area. **This behavior is**
 379 **opposite of that observed in the non-irradiated sensors, both CNM and HPK.**
 380 However, given that the signals in the non-metallized area of the irradiated
 381 CNM sensor are much larger than those in the periphery, this behavior is
 382 expected, since the gain in this region is larger (is it?).

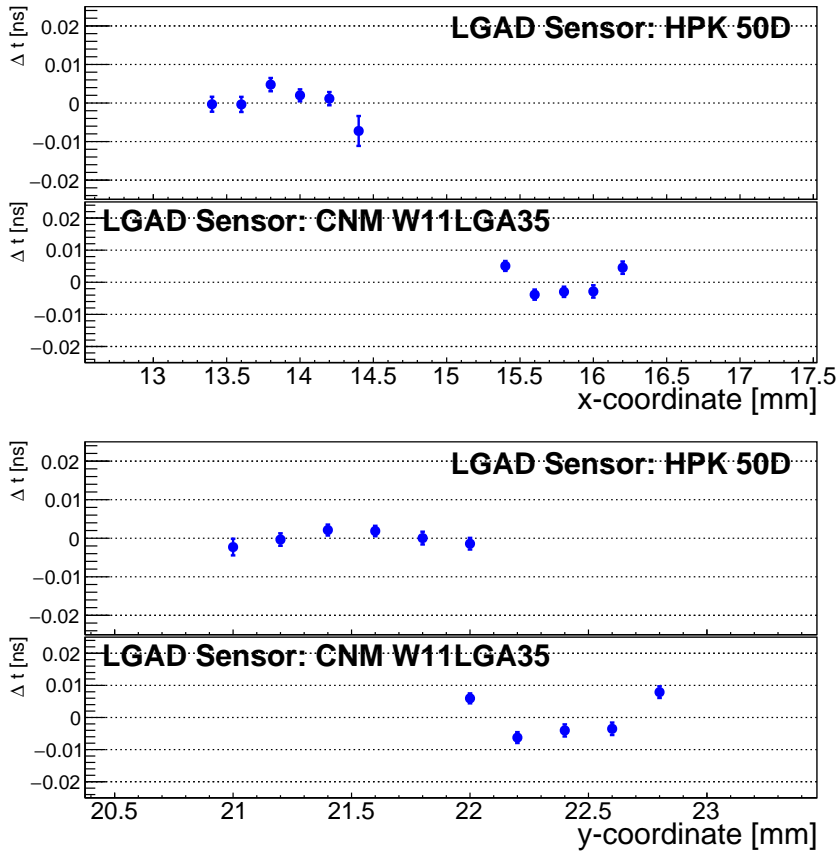


Figure 22: Δt measurements across the X-axis (top) and Y-axes (bottom) of the HPK 50D and CNM W11LGA35 irradiated sensors. Both sensors were irradiated to $6 \times 10^{14} \text{ n/cm}^2$. Measurements were performed at -20°C .

383 Distributions of the time resolution across the surface of the irradiated sensors are
 384 shown in Fig. 23. The time resolution measured with the HPK sensor improves slightly
 385 with the increase of the bias voltage, and shows a uniform distribution across the sensor
 386 surface. In contrast, the CNM sensor shows a non-uniform distribution of time resolution,
 387 which is a consequence of the variations of the signal amplitude across the sensor. We
 388 do not observe an improvement in the time resolution measured with the CNM sensor

³⁸⁹ with the increase in the bias voltage.

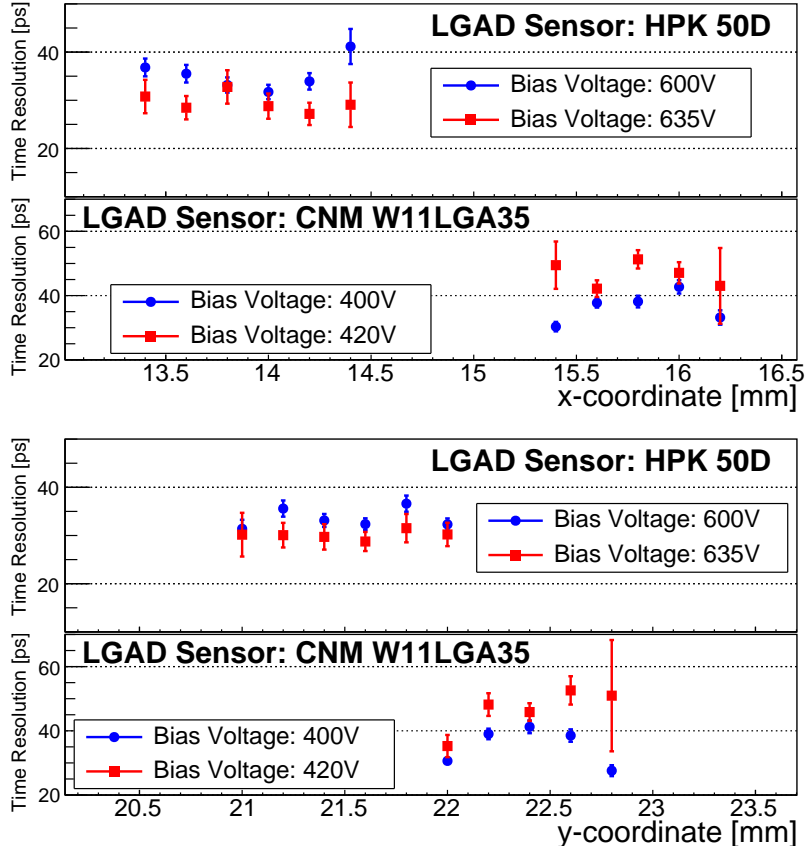


Figure 23: Time resolution measurements across the X-axis (top) and Y-axes (bottom) of the HPK 50D and CNM W11LGA35 irradiated sensors. Both sensors were irradiated to $6 \times 10^{14} \text{ n/cm}^2$. Measurements were performed at -20°C .

³⁹⁰ 6. Conclusion

³⁹¹ In a beam test at FNAL with tracking information, we compared the performance
³⁹² of LGAD produced by CNM Barcelona and HPK Hamamatsu. Single pads of diameter
³⁹³ 1 mm and 2×2 arrays of square pixels of 3 mm were used. Sensors with thicknesses of
³⁹⁴ about 50 and $80 \mu\text{m}$ were studied. Four different readout boards were used, and their
³⁹⁵ performance characteristics are to be discussed in detail in an upcoming paper []. The
³⁹⁶ uniformity of the sensor response in pulse height, efficiency, and timing resolution were
³⁹⁷ studied. The uniformity of the sensor response in pulse height before irradiation was
³⁹⁸ found to have a 2% spread. The efficiency and timing resolution before irradiation were
³⁹⁹ found to be 100% and 30-40 ps, respectively. The “non-response” region between pixels
⁴⁰⁰ was measured to be about 70 μm for CNM sensors and 110 μm for HPK sensors. A

401 small timing shift across the HPK sensor of the order 20–30 ps' can be explained by the
402 observed change in pulse shape when comparing metallized and non-metallized sensor
403 areas. Uniform signal detection efficiency of 100% is observed on all sensors, both before
404 and after irradiation.

405 For an un-irradiated 50 μm thick LGADs with 3 mm pads we find the following timing
406 results:

- 407 • at a temperature of +20°C, the timing resolution ranges from 40 ps to 50 ps
408 depending on the readout board.
- 409 • cooling the LGAD, while keeping the bias voltage the same at -250 V (**what is**
410 **the gain at -250 V**), improves the timing resolution from 55 ps at +20°C to
411 43 ps at -10°C to 36 ps at -20°C.

412 After a neutron fluence of $6 \times 10^{14} \text{ n/cm}^2$, the single pad CNM sensor exhibits a
413 large gain variation of a factor 2.5 when comparing metallized and non-metallized sensor
414 areas. For an 50 μm thick LGAD with 1 mm pads irradiated $6 \times 10^{14} \text{ n/cm}^2$ we find the
415 following timing results when operated at -20°C:

- 416 • for the HPK LGAD the highest bias voltage reached is -635 V and the correspond-
417 ing timing resolution is 30 ps;
- 418 • for the CNM LGAD the highest bias voltage reached is -420 V and the correspond-
419 ing timing resolution is 30 ps for the metallized area and 40 ps for the non-metallized
420 area.

421 Acknowledgement

422 We thank the FTBF personnel and Fermilab accelerator's team for very good beam
423 conditions during our test beam time. We also appreciate the technical support of the
424 Fermilab SiDet department for the rapid production of wire-bonded and packaged LGAD
425 assemblies. We would like to thank Alan Prosser and Ryan Rivera for their critical help
426 in setting up the DAQ and trigger chain. We thank Ned Spencer, Max Wilder, and Forest
427 McKinney-Martinez for their technical assistance, and the CNM and HPK manufacturing
428 team. We acknowledge the help of V. Cindro and I. Mandic with the neutron irradiations.

429 This document was prepared using the resources of the Fermi National Accelerator
430 Laboratory (Fermilab), a U.S. Department of Energy, Office of Science, HEP User
431 Facility. Fermilab is managed by Fermi Research Alliance, LLC (FRA), acting under
432 Contract No. DE-AC02-07CH11359. Supported by funding from California Institute of
433 Technology High Energy Physics under Contract DE-SC0011925 with the United States
434 Department of Energy.

435 Part of this work has been performed within the framework of the CERN RD50 Col-
436 laboration. The work was supported by the United States Department of Energy, grant
437 DE-FG02-04ER41286, and Fermilab LDRD 2017.027. Part of this work was supported
438 by funding from the California Institute of Technology High Energy Physics under Con-
439 tract DE-SC0011925 with the United States Department of Energy. Part of this work has
440 been financed by the European Unions Horizon 2020 Research and Innovation funding
441 program, under Grant Agreement no. 654168 (AIDA-2020) and Grant Agreement no.

442 669529 (ERC UFSD669529), and by the Italian Ministero degli Affari Esteri and INFN
 443 Gruppo V.

444 The list of sensors studied in this article, as well as the temperature and the sensor
 445 bias voltage used during their operation are listed in Tab. 1.

Sensor	KU Board 2-ch	UCSC board 4-ch	FNAL board 4-ch
HPK 50A-PIX	-630 V (13)	—	—
HPK 50B-PIX	-450 V (10), -550 V (25), -600 V (60) — <u>-510 V</u> <u>-510 V, -570 V</u>	—	—
HPK 50C-PIX	-400 V (20)	-410 V (22), -470 V (40)	—
HPK 50D-PIX	-100 V (7), -200V (11), -250 V (17), -300 V (30), -325 V (40)	—	-250 V (17), -300 V (30), -210 V, -250 V -250 V (30), -280 V (40)
CNM W9HG11	—	-140 V, -160V	—
HPK 50D $6 \times 10^{14} \text{ n/cm}^2$	—	-600 V (20), -635 V (30)	—
CNM W11LGA35 $6 \times 10^{14} \text{ n/cm}^2$	—	—	-400 V, -420 V

Table 1: Data taking conditions for the studies presented in this paper. Numbers in bold indicate that the sensor was at room temperature, underlined ones were taken at -10°C , and those in italicized text were taken at -20°C .

446 References

- 447 [1] A. Apresyan, G. Bolla, A. Bornheim, H. Kim, S. Los, C. Pena, E. Ramberg, A. Ronzhin, M. Spiropulu, and S. Xie, “Test beam studies of silicon timing for use in calorimetry,” *Nuclear Instruments and Methods in Physics Research Section A: Accelerators, Spectrometers, Detectors and Associated Equipment*, vol. 825, pp. 62 – 68, 2016.
- 451 [2] A. Apresyan, “Investigation of Fast Timing Capabilities of Silicon Sensors for the CMS High Granularity Calorimeter at HL-LHC,” in *Proceedings, 2016 IEEE Nuclear Science Symposium and Medical Imaging Conference (NSS/MIC 2016)*, Oct 2016. <http://2016.nss-mic.org/index.php>.
- 455 [3] N. Akchurin, V. Ciriolo, E. Currs, J. Damgov, M. Fernndez, C. Gallrapp, L. Gray, A. Junkes, M. Mannelli, K. M. Kwok, P. Meridiani, M. Moll, S. Nourbakhsh, S. Pigazzini, C. Scharf, P. Silva, G. Steinbrueck, T. T. de Fatis, and I. Vila, “On the timing performance of thin planar silicon sensors,” *Nuclear Instruments and Methods in Physics Research Section A: Accelerators, Spectrometers, Detectors and Associated Equipment*, vol. 859, pp. 31 – 36, 2017.
- 459 [4] N. Cartiglia *et al.*, “Beam test results of a 16 ps timing system based on ultra-fast silicon detectors,” *Nucl. Instrum. Meth. A*, vol. 850, pp. 83 – 88, 2017.
- 463 [5] S. Kwan, C. Lei, D. Menasce, L. Moroni, J. Ngadiuba, A. Prosser, R. Rivera, S. Terzo, M. Turqueti, L. Uplegger, L. Vigani, and M. E. Dinardo, “The pixel tracking telescope at the fermilab test beam facility,” *Nuclear Instruments and Methods in Physics Research Section A: Accelerators, Spectrometers, Detectors and Associated Equipment*, vol. 811, pp. 162 – 169, 2016.
- 467 [6] D. Anderson, A. Apresyan, A. Bornheim, J. Duarte, C. Pena, A. Ronzhin, M. Spiropulu, J. Trevor, and S. Xie, “On Timing Properties of LYSO-Based Calorimeters,” *Nucl. Instrum. Meth. A*, vol. 794, pp. 7–14, 2015.
- 471 [7] A. Ronzhin, S. Los, E. Ramberg, M. Spiropulu, A. Apresyan, S. Xie, H. Kim, and A. Zatserklyaniy, “Development of a new fast shower maximum detector based on microchannel plates photomultipliers (MCP-PMT) as an active element,” *Nucl. Instrum. Meth. A*, vol. 759, pp. 65 – 73, 2014.
- 475 [8] A. Ronzhin, S. Los, E. Ramberg, A. Apresyan, S. Xie, M. Spiropulu, and H. Kim, “Study of the timing performance of micro-channel plate photomultiplier for use as an active layer in a shower maximum detector,” *Nucl. Instrum. Meth. A*, vol. 795, pp. 288 – 292, 2015.
- 479 [9] A. Ronzhin, S. Los, E. Ramberg, A. Apresyan, S. Xie, M. Spiropulu, and H. Kim, “Direct tests of micro channel plates as the active element of a new shower maximum detector,” *Nucl. Instrum. Meth. A*, vol. 795, pp. 52 – 57, 2015.

- 477 [10] <http://www.caen.it/csite/CaenProd.jsp?parent=11&idmod=661>.
- 478 [11] H. Kim, C.-T. Chen, N. Eclov, A. Ronzhin, P. Murat, E. Ramberg, S. Los, W. Moses, W.-S. Choong,
479 and C.-M. Kao, “A new time calibration method for switched-capacitor-array-based waveform sam-
plers,” *Nucl. Instrum. Meth. A*, vol. 767, pp. 67 – 74, 2014.
- 480 [12] M. Carulla et al, “First 50 m thick LGAD fabrication at CNM.” <https://agenda.infn.it/getFile.py/access?contribId=20&sessionId=8&resId=0&materialId=slides&confId=11109>, 2016. 28th
481 RD50 Workshop, Torino.
- 482
- 483